ACS OMEGA

Article

Cite This: ACS Omega 2019, 4, 5714−5721

http://pubs.acs.org/journal/acsodf

Mechanical, Electronic, and Magnetic Properties of NiX_2 (X = Cl, Br, I) Layers

Min Lu,[†] Qiushi Yao,[‡] Chuanyun Xiao,[†] Chengxi Huang,*[,†] and Erjun Kan*[,†]

[†]Department of Applied Physics and Institution of Energy and Microstructure, Nanjing University of Science and Technology, Nanjing, Jiangsu 210094, P. R. China

[‡]Department of Physics and Shenzhen Institute for Quantum Science and Technology, Southern University of Science and Technology, Shenzhen 518055, China

ABSTRACT: Since the recent experimental discovery of the CrI_3 and $CrGeTe_3$ monolayers, van der Waals (vdW) layered transition metal compounds have been recognized as promising candidates to realize 2D ferromagnetic (FM) semiconductors. However, until now, only limited compounds have been proposed to be ferromagnetic semiconductors. Here, on the basis of first-principles calculations, we report that the monolayer, Janus monolayer, and bilayer of NiX_2 (X = Cl, Br, I) are intrinsic 2D FM semiconductors. Our results show that exfoliation energy of the NiX_2 monolayer is smaller than that of graphene, and all studied NiX_2 layers show semiconducting band gaps. The predicted Curie temperature values for NiX_2 (X = Cl, Br, I) monolayers ranged from 120 to 170 K with Monte Carlo simulations. For the Janus monolayer, we found that the spin interaction shows a very strong magnetoelectric coupling under an external electric field. Furthermore, for the bilayer of NiX_2, our results show that the interlayer coupling is quite weak, indicating the possibility of tuning the magnetic coupling through external manipulations.

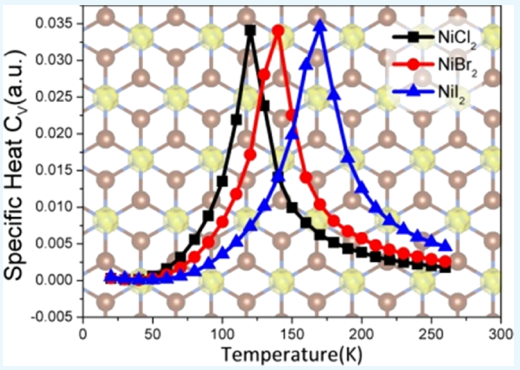

INTRODUCTION

During the past decade, two-dimensional (2D) materials, such as graphene,[1] h-BN,[2] MoS_2,[3] and black phosphorus,[4] have received much attention because of their unique properties and potential applications in future nanodevices.[5] Magnetism, especially in 2D systems, is one of the most fascinating properties of materials, not only because of the complex magnetic behavior itself but also due to its interplay with the other important properties of materials such as superconductivity, ferroelectricity, and quantum Hall effects. However, in early studies, long-range magnetic order is predicted to be prohibited in a 2D system according to the Mermin−Wagner theorem.[6] Recently, Gong et al.[7] and Huang et al.[8] reported their discovery of long-range ferromagnetic (FM) order in 2D intrinsic semiconductors, $Cr_2Ge_2Te_6$ and CrI_3, which are exfoliated down to atomically thin layers from their van der Waals (vdW) layered bulk materials. These exciting findings promote the studies of 2D magnetic semiconductors to a new stage. But the measured Curie temperature (T_C) values of these materials are very low (<45 K), which badly hinders their practical applications in spintronic devices.

Tremendous efforts have been devoted to realize ferromagnetic order in 2D semiconductors with higher Curie temperature. For example, embedding transition metal atoms and applying strain, defects, or boundaries[9−13] have been adopted as a strategy to induce magnetism in a nonmagnetic system. But these methods are usually difficult to control in an experiment, and the induced ferromagnetism is very weak. Recently, the vdW layered transition metal compounds have been recognized as promising candidates to realize 2D FM semiconductors because these materials usually possess intrinsic magnetism and can be easily exfoliated down to monolayers. Several 2D systems have been confirmed to be intrinsic FM materials such as VSe_2,[14] $MnSe_2$,[15] $FePS_3$,[16] and MnO_2,[17] but all these materials are metallic. 2D FM semiconductors are still very rare, and their T_C values are much below room temperature because the virtual exchange interactions in a semiconductor are usually much weaker than the carrier-driven exchange interactions in a metallic system. Thus, to better understand the intrinsic mechanism of ferromagnetic semiconductors, it becomes more and more important to explore new families of semiconducting monolayers with ferromagnetism.

Here, on the basis of first-principles calculations, we predict that the family of NiX_2 (X = Cl, Br, I) layers can be promising 2D intrinsic FM semiconductors. Our results show that exfoliation energy of the NiX_2 monolayer is smaller than that of graphene, and all the NiX_2 monolayers show semiconducting band gaps, which vary from 1.24 to 2.60 eV.

Received: January 7, 2019
Accepted: March 6, 2019
Published: March 22, 2019

DOI: 10.1021/acsomega.9b00056
ACS Omega 2019, 4, 5714−5721

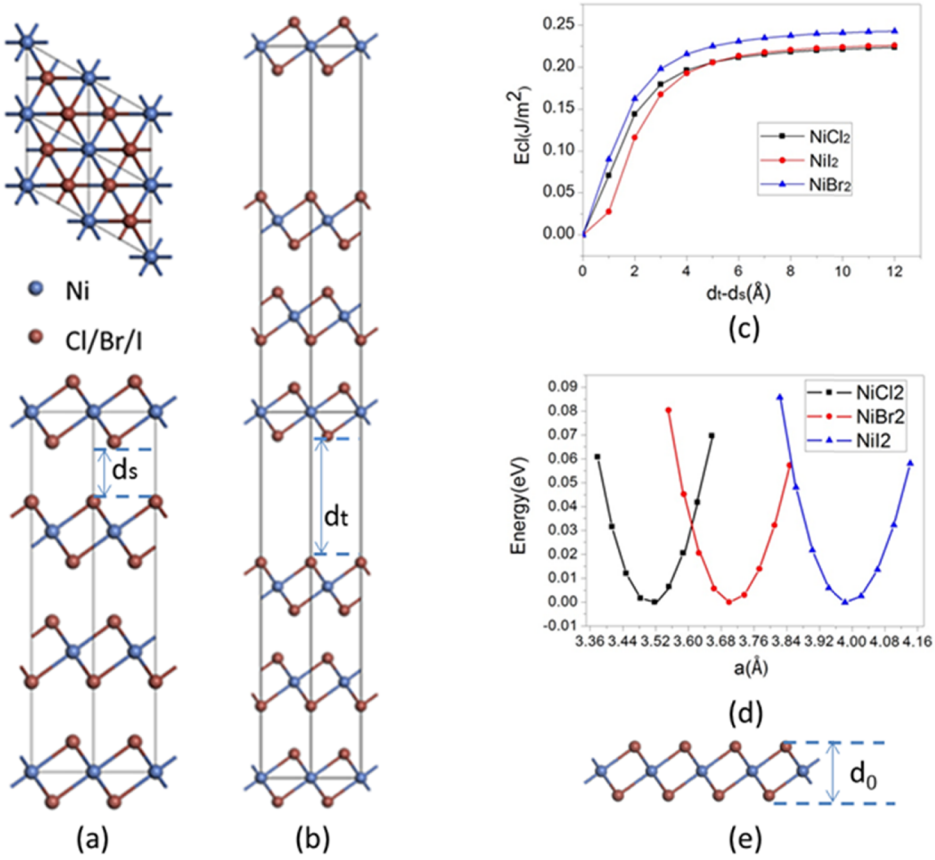

Figure 1. (a) Top (upper panel) and side (bottom panel) views of crystal structure of bulk NiX_2 (X = Cl, Br, I). (b) Super cell model with introduced fracture used to simulate the exfoliation procedure. (c) Cleavage energy E_{cl} as a function of the separation between two fractured parts. (d) Variation of relative energy with the 2D lattice constant for the monolayer of NiX_2. The energy of equilibrium state is set to 0. (e) NiX_2 monolayer. d_0 is the vertical distance between two halide atomic planes.

Their Curie temperature (T_C) values were predicted from 120 to 170 K with Monte Carlo simulations. For the Janus monolayer, we found that the spin interaction shows a very strong magnetoelectric coupling. Furthermore, for the bilayer of NiX_2, our results show that the interlayer coupling is quite weak, indicating the possibility of tuning the magnetic coupling through external manipulations.

RESULTS AND DISCUSSION

The large interlayer distance between vdW layers (3.08, 3.28, and 3.35 Å for $NiCl_2$, $NiBr_2$, and NiI_2, respectively) of NiX_2 bulks implies a weak interlayer interaction between layers and the possibility to obtain 2D monolayers with a suitable exfoliation method. To demonstrate this, two fundamental questions should be taken into account. One is the cleavage energy, which gives a quantitative description of the strength of interlayer binding, and the other one is the in-plane stiffness of the corresponding 2D monolayer, which determines whether the exfoliated monolayer can have a large area and be free-standing. Generally, a small cleavage energy and strong in-plane stiffness are what we need.

To achieve the 2D monolayer from the vdW bulk crystals, the most commonly used approaches are mechanical cleavage and liquid exfoliation.[1,18,19] To confirm that it is possible to exfoliate NiX_2 monolayers from their bulk phases in the experiment, we first calculated the cleavage energy. A gradually expanded fracture is introduced in the bulk to simulate the exfoliation procedure (Figure 1a,b).[20] As expected, the total energy increases as the separation between two fractured parts increases (Figure 1c). It can be found that the total energy increases rapidly when the separation is less than 3.0 Å. As the separation becomes larger, the total energy barely changes. Then, we find that the cleavage energies for $NiCl_2$, $NiBr_2$, and NiI_2 are 0.223, 0.242, and 0.26 J/m^2, which are smaller than that for graphite (~0.36 J/m^2),[21,22] implying that NiX_2 can be easily exfoliated down to the monolayer in the experiment. We also calculate the cleavage energy of bilayer nanosheets and obtain very similar values, which are 0.224, 0.243, and 0.26 J/m^2.

To obtain a free-standing membrane during the exfoliation process in the experiment, it is important to avoid curling or buckling. To investigate the in-plane stiffness of NiX_2 monolayers, the 2D Young's modulus is evaluated according to the following equation

$$Y_{2D} = A_0\left(\frac{(\partial^2 E)}{\partial A^2}\right)_{A_0} = \frac{1}{2\sqrt{3}}\left(\frac{(\partial^2 E)}{\partial a^2}\right)_{a_0}$$

where E is the total energy per unit cell, a_0 is the 2D lattice constant, and A is the corresponding surface area. Figure 1d shows the profile of total energy versus lattice constant a_0 for NiX_2 monolayers. The 2D Young's moduli for $NiCl_2$, $NiBr_2$, and NiI_2 are calculated to be 54, 50, and 45 N m^{-1}, respectively, which are close to that of the $MnPSe_3$[23] monolayer and comparable to that of the ultrastrong material graphene (~340 N m^{-1}).[24,25] Further, according to the elastic

DOI: 10.1021/acsomega.9b00056
ACS Omega 2019, 4, 5714−5721

theory, the typical out-of-plane deformation h induced by gravity can be estimated by the formula[25]

$$\frac{h}{L} \approx \left(\frac{pgL}{Y_{2D}}\right)^{1/3}$$

where $p = 2.00 \times 10^{-6}$, 3.06×10^{-6}, and 3.78×10^{-6} kg/m^2 are the densities of 2D $NiCl_2$, $NiBr_2$, and NiI_2, respectively, and L is the edge length. Assuming that $L \approx 100$ μm, we obtain h/L values of 3.31×10^{-4}, 3.91×10^{-4}, and 4.35×10^{-4} for 2D $NiCl_2$, $NiBr_2$, and NiI_2, respectively. These values are of the same order of magnitude as that of graphene.[25] These suggest that the NiX_2 monolayers are stiff enough to withstand its own weight and keep a free-standing planar structure during exfoliation.

The NiX_2 monolayers possess a structure similar to that of the T-MoS_2 monolayer, which belong to the P-3m1 layer group. No Jahn−Teller distortion is observed, and each Ni atom is coordinated to six ligands. The structural parameters are listed in Table 1. As the atomic radius increases from $NiCl_2$ to NiI_2, the lattice constant a_0, bond length of Ni−X atom marked as d_{Ni-X}, and vertical distance between two halide planes d_0 also increase. The calculated lattice constants a_0 of the monolayers are very close to those of their bulks (3.483, 3.699, and 3.983 Å for $NiCl_2$, $NiBr_2$, and NiI_2, respectively), suggesting very weak interlayer interactions between vdW layers.

Table 1. Geometrical Parameters of Optimized Monolayers NiX_2 (X = Cl, Br, I), Lattice Constant (a_0), Bond Length between Atoms Ni and X (d_{Ni-X}), and Interlayer Distance between Two Halide Planes (d_0)

compound	a_0 (Å)	d_{Ni-X} (Å)	d_0 (Å)
$NiCl_2$	3.518	2.424	2.648
$NiBr_2$	3.700	2.573	2.868
NiI_2	3.983	2.775	3.107

In NiX_2 monolayers, because of the octahedral crystal field caused by the ligands, the Ni d orbitals split into two parts, namely, the lower t_{2g} and the higher e_g manifolds. Each Ni gives two electrons to form ionic bonding with the ligands and leaves eight electrons, which fully occupy the t_{2g} orbitals and the spin-up e_g orbitals, and the spin-down e_g orbitals are empty. Thus, the Ni^{2+} ion shows an occupation state of d^8 with a magnetic moment of ~2 μ_B. A sizable electronic band gap is expected to be opened by the crystal field. To determine the magnetic ground state of monolayer NiX_2, we carry out spin-polarized calculations. Two different magnetic configurations are considered in a 2 × 1 super cell, that is, the FM state and antiferromagnetic (AFM) state. The spin densities for these two states are shown in Figure 2a,b. The spin polarizations are mainly contributed by Ni ions, while the ligands are slightly spin-polarized. The projected magnetic moment on each Ni ion is nearly the same for FM and AFM states. The numerical results are listed in Table 2. It is found that the FM states for $NiCl_2$, $NiBr_2$, and NiI_2 monolayers are lower in energy than the corresponding AFM states by 11.2, 12.6, and 15.4 meV per unit cell, respectively, suggesting that the ground states are FM; this is consistent with recent studies reported by Mounet et al.[26]

It is known that the results from GGA + U calculations for a magnetic system sometimes may depend on the adopted value of effective Hubbard U (U_{eff}). Thus, to verify our result, we repeat the GGA + U calculations with U_{eff} = 2−5 eV for Ni d orbitals for the NiI_2 monolayer. The ground state remains FM with exchange energy ranging from 12 to 23 meV. Thus, the predicted ferromagnetism in NiI_2 is robust against the value of Hubbard U.

Figure 3 shows the electronic structures of FM ground states for NiX_2 monolayers. Here, we focus on the results calculated by the PBE + U method. The effect of spin-orbit coupling (SOC) can be further elucidated by comparing the electronic band structure, as shown in Figure 3. It is found that all the three systems are semiconductors with indirect band gaps of 2.60, 1.97, and 1.24 eV for $NiCl_2$, $NiBr_2$, and NiI_2, respectively, consistent with our above analysis. The decrease in band gap from $NiCl_2$ to NiI_2 is due to the decrease in strength of the crystal field, which is inversely proportional to the Ni−X bond length. Interestingly, the value of exchange energy increases from $NiCl_2$ to NiI_2. This may be caused by two factors: (i) The reduction of energy gap between t_{2g} and e_g orbitals will strengthen the t_{2g}−e_g virtual exchange interaction, benefiting the FM coupling, which has been carefully discussed in our previous work.[27] (ii) I has a smaller electronegativity than Cl, namely, the on-site energy of I p orbitals is closer to that of Ni d orbitals than the Cl p orbitals do. Thus, the d−p−d superexchange in NiI_2 is stronger than that in $NiCl_2$, which can be confirmed by comparing the PDOS between NiI_2 and $NiCl_2$, where the broadening of Ni d orbitals in energy for NiI_2 is larger than that for $NiCl_2$. Similar phenomena are also found in previous studies on transition metal halides monolayers such as CrX_3[28] and VX_3.[29] After considering SOC, there is no noticeable change in the electronic band structure, as shown in Figure 3, with the indirect band gaps of 2.57, 1.82, and 1.03 eV for $NiCl_2$, $NiBr_2$, and NiI_2, respectively.

For practical spintronic applications of 2D FM semiconductors, it is necessary to investigate the magnetic behavior under finite temperature. The Ising model has been widely used to describe the magnetic coupling in 2D magnetic systems.[17,30−32] Here, we also use the Ising model including nearest-neighboring exchange interactions to study the magnetic behavior of NiX_2 (X = Cl, Br, I) monolayers. The spin Hamiltonian

$$H = -\sum_{\langle i,j \rangle} J_{ij} S_i S_j$$

where the summation i runs over all Ni sites, j runs over the six nearest neighbors of site i. J_{ij} is the nearest-neighboring exchange parameter. Then, we performed Metropolis Monte Carlo simulations[33,34] to estimate the T_C. A 30 × 30 hexagonal superlattice containing 900 magnetic sites and the periodic boundary condition is used. The average magnetization per formula unit and the specific heat [$C_v = (\langle E^2 \rangle - \langle E \rangle^2)/k_B T^2$] are taken after the system reaches the equilibrium state at a given temperature (Figure 4). The T_C can also be extracted from the peak of the specific heat profile.[35] The estimated T_C values for NiX_2 (X = Cl, Br, I) monolayers are 120, 140, and 170 K, respectively, which are much larger than the reported values for 2D CrI_3 (~45 K)[8] and $Cr_2Ge_2Te_6$ (~30 K)[7] and are higher than the liquid nitrogen temperature (77 K).

For practical uses, a 2D material usually needs to be supported by a suitable substrate, which may apply an in-plane strain and affect the performance of the pristine material. Thus, it is necessary to investigate the magnetic and electronic properties of NiX_2 monolayers under a proper in-plane strain.

DOI: 10.1021/acsomega.9b00056
ACS Omega 2019, 4, 5714−5721

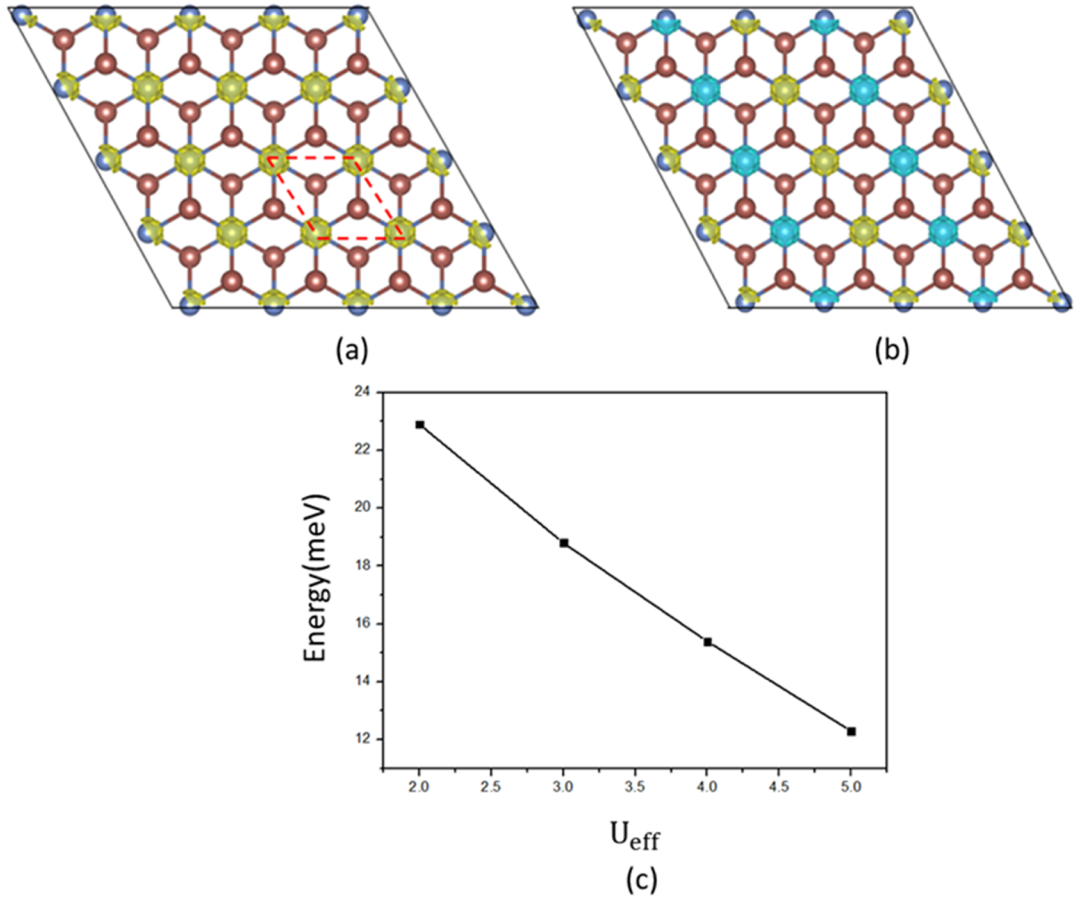

Figure 2. Spin density (isovalue of 0.025 e/Å^3) of (a) the FM state and (b) AFM state. Yellow and blue isosurfaces represent net spin-up and spin-down charge densities, respectively. The rhombic primitive cell is marked by a red dotted line. (c) Change of exchange energy of monolayer NiI_2 with respect to different values of U_{eff}.

Table 2. Projected Magnetic Moment on Each Ni Site (M_u), Exchange Energy (E_{ex}), Electronic Band Gap (E_g), Nearest-Neighboring Exchange Parameter (J), and Curie Temperature (T_C)

compound	M_u (μ_B)	E_{ex} (eV)	E_g (eV)	J (meV)	T_C (K)
$NiCl_2$	1.63	11.2	2.60	2.8	~120
$NiBr_2$	1.57	12.6	1.97	3.2	~140
NiI_2	1.46	15.4	1.24	3.9	~170

Here, we focus on NiI_2 because it has the highest T_C among the three systems. The applied biaxial in-plane strain is defined as $\varepsilon = (a - a_0)/a_0 \times 100\%$, where a_0 and a are the lattice constants of 2D NiI_2 in its equilibrium and strained states, respectively. Positive and negative values of ε represent tensile and compressive strain, respectively. As shown in Figure 5a, a tensile strain will reduce the exchange energy. This is opposite to previous studies on CrI_3[28] and $CrGeTe_3$[36] where the exchange energy is increased by a tensile strain. It can be understood that the Cr^{3+} ion in CrI_3 and $CrGeTe_3$ has a d^3 occupation state, which is less than half-filled. In this case, the AFM direct exchange mainly contributed by the $t_{2g}-t_{2g}$ hybridizations, which can be fairly reduced by a tensile in-plane strain that increases the distance between neighboring Cr^{3+} ions. Thus, a proper tensile in-plane strain can enhance the FM couplings in CrI_3 and $CrGeTe_3$. But in NiI_2, the occupation state of Ni^{2+} (d^8) is more than half-filled. In this case, the AFM direct exchange originates from e_g-e_g hybridizations, which is usually much weaker than the $t_{2g}-t_{2g}$ hybridizations and is not sensitive to a tensile strain, while the tensile strain reduces the d−p exchange interactions, weakening the FM couplings between adjacent Ni^{2+} ions. When applying a compressive strain, the exchange energy decreases. This is mainly because a compressive strain will strengthen the crystal field, increasing the energy gap between t_{2g} and e_g orbitals (Figure 5c) and weakening the FM $t_{2g}-e_g$ virtual exchange interactions. The indirect band gaps of NiI_2 under −4 and 4% strain are 0.90 and 1.43 eV, respectively. Overall, the electronic and magnetic properties of NiI_2 only slightly change under a moderate in-plane strain, which makes it a robust 2D FM semiconductor. PBE functional is known to usually underestimate the band gap; thus, we also repeat our calculation using HSE06 hybrid functional for NiI_2 monolayer. The band structure of NiI_2 calculated by HSE06 functional is also shown in Figure 5b, with an indirect band gap of 2.31 eV nearly twice as large as the one (1.24 eV) calculated by the PBE + U method. Also, the ground state is also FM with an exchange energy of 19.5 meV, which is a bit larger than the PBE + U result (15.4 meV).

Janus 2D materials with breaking mirror or inversion symmetry along out-of-plane orientations provide abundant new properties such as electric polarization and Rashba effect, which expands the promising applications of 2D materials.[37−39] Thus, it will be interesting to explore the properties of the Janus NiXY monolayer. Here, we calculated the NiICl monolayer. The calculated lattice constant is 3.74 Å, which is

DOI: 10.1021/acsomega.9b00056
ACS Omega 2019, 4, 5714−5721

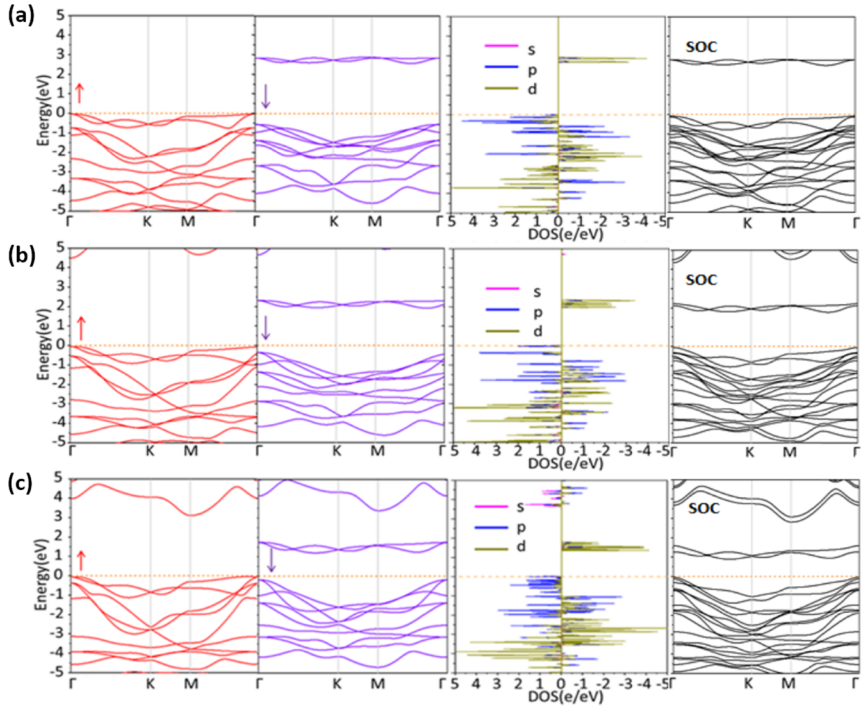

Figure 3. Band structure and corresponding density of states of (a) $NiCl_2$, (b) $NiBr_2$, and (c) NiI_2 monolayers.

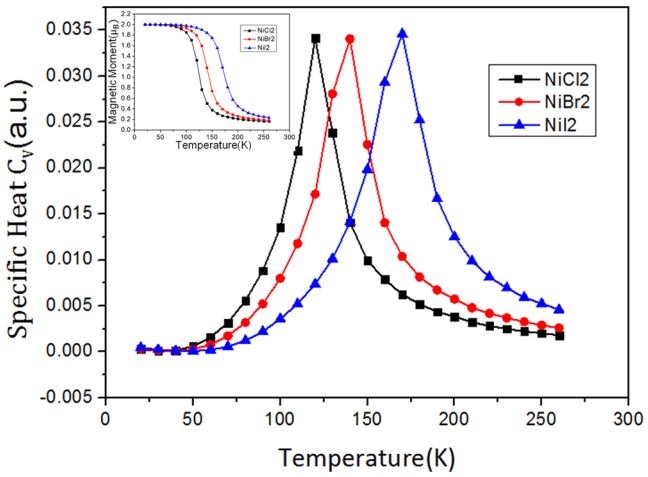

Figure 4. Specific heat C_v with respect to temperature for the $NiCl_2$, $NiBr_2$, and NiI_2 monolayers; the inset shows the corresponding magnetization.

between those of NiI_2 and $NiCl_2$. The breaking of inversion symmetry can be seen from the optimized structure (Figure 6a). This induces a vertical electric polarization of 0.19 C/m^2, making NiICl a 2D multiferroic material. The magnetic ground state is also FM for NiICl, with an exchange energy of 9.3 meV. Interestingly, because of out-of-plane electric polarization, the response of magnetic coupling to a vertical external electric field also exhibits a "polar" behavior; that is, an electric field along the $+z$ direction will enhance the FM coupling, while an electric field along the $-z$ direction will weaken it (Figure 6b). On the other hand, the electronic structure of NiICl does not change much compared to that of the NiI_2 monolayer (Figure 6c).

On the other hand, 2D magnetic materials are usually used as a building block of vdW heterostructures and junctions to realize a highly functional nanodevice. For instance, the recently discovered 2D FM semiconductor CrI_3 shows AFM interlayer magnetic couplings in bilayer CrI_3. This unusual property has attracted much attention. Thus, it is also important to explore the interlayer interactions between NiX_2 layers. Here, AA- and AB-stacked bilayers of $NiCl_2$, $NiBr_2$, and NiI_2 are considered in our calculations. The AB-stacked bilayers are more favored than the AA-stacked ones with total energy values lower by 0.001, 0.001, and 0.002 eV for $NiCl_2$, $NiBr_2$, and NiI_2, respectively. The lattice constants a_0 of AB-stacked bilayers $NiCl_2$, $NiBr_2$, and NiI_2 are 3.49, 3.70, and 4.01 Å, which are very close to their bulks, suggesting weak vdW interlayer interactions between layers.

For the magnetic coupling in such bilayer systems, two different magnetic configurations are considered, that is, the FM state and the interlayer-antiferromagnetic (I-AFM, where Ni ions in one layer possess spin-up magnetic moment and, in the other layer, possess spin-down magnetic moment) state. We find that the FM states are lower in energy than the I-AFM states. But the energy differences between FM and I-AFM states are very small, which are 0.27, 0.65, and 2.20 meV for AB stacking (0.17, 0.47, and 1.42 meV for AA stacking), suggesting that the magnetic coupling between NiX_2 layers can be easily tuned by external perturbations.

CONCLUSIONS

In summary, on the basis of first-principles calculations, we propose a class of 2D FM semiconductors, the NiX_2 (X = Cl, Br, I) monolayers by exfoliation from corresponding vdW bulk materials. The calculated cleavage energy of bulk NiX_2 (X = Cl, Br, I) is slightly smaller than that of graphite, indicating that exfoliation is possible in the experiment by mechanical cleavage or liquid exfoliation. Meanwhile, the calculated in-plane stiffness implies that the 2D NiX_2 (X = Cl, Br, I) monolayers can keep their free-standing structures without curling or buckling. All three monolayers are semiconducting with band gaps of 2.60, 1.97, and 1.24 eV for $NiCl_2$, $NiBr_2$, and

DOI: 10.1021/acsomega.9b00056
ACS Omega 2019, 4, 5714−5721

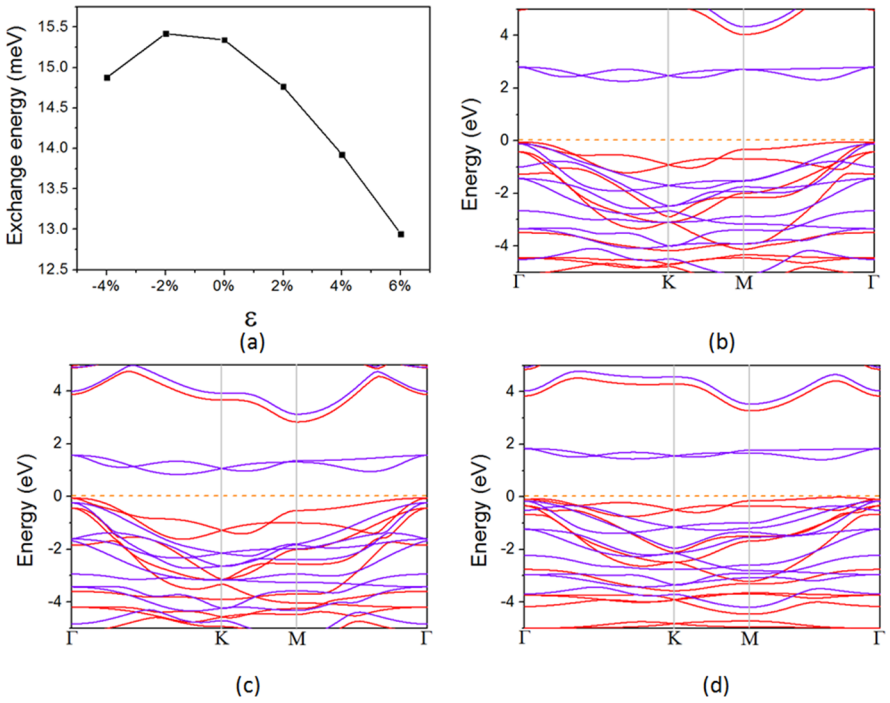

Figure 5. (a) Change of exchange energy with respect to the in-plane biaxial strain. (b) Band structure of NiI_2 calculated by HSE06 hybrid functional. (c) Band structure of NiI_2 under −4% strain. (d) Band structure of NiI_2 under 4% strain. The red and purple lines represent the spin-up and spin-down bands, respectively.

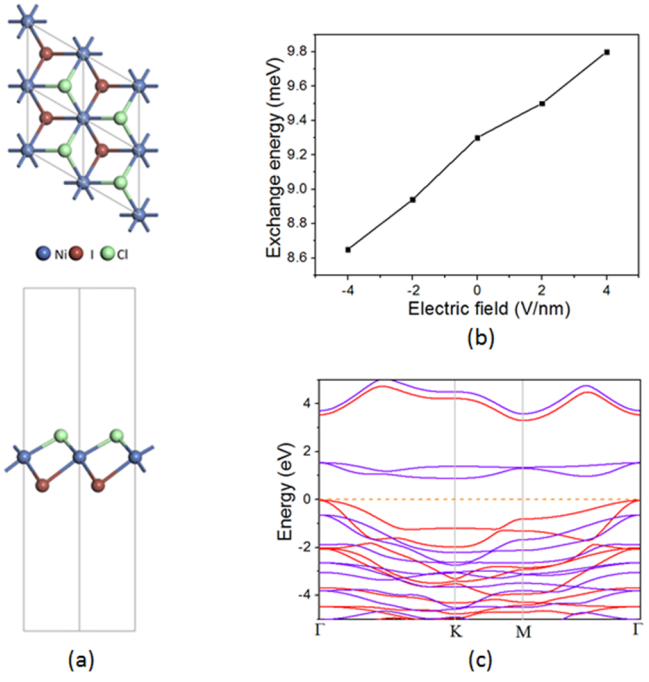

Figure 6. (a) Top (upper panel) and side (bottom panel) views of crystal structure of NiICl. (b) Change of exchange energy with respect to electric field. (c) Band structure of NiICl. The red and purple lines represent the spin-up and spin-down bands, respectively.

NiI_2, respectively. The ground states of the monolayers are FM with T_C values ranging from 120 to 170 K. The T_C increases from $NiCl_2$ to $NiBr_2$ and NiI_2 due to enhanced p−d exchange interactions and t_{2g}−e_g virtual exchange interactions. Different from the usual case of tensile strain-induced enhancement of ferromagnetism in systems such as CrI_3 and $CrGeTe_3$, FM couplings in NiI_2 are slightly decreased by both tensile and compressive strain due to its more than half-filled occupation state. Besides, for the Janus monolayer, we found that the spin interaction shows a very strong magnetoelectric coupling. Furthermore, for the bilayer of NiX_2, our results show that the interlayer coupling is quite weak, indicating the possibility of tuning the magnetic coupling through external manipulations. Our findings suggest that NiX_2 (X = Cl, Br, I) layers can have promising applications in spintronic devices such as spin valves, information transport, and storage between electric signals and spin signals. We hope that the present study will stimulate further experimental effort on this subject.

COMPUTATIONAL METHODS

The first-principles calculations based on spin-polarized density functional theory (DFT) are performed using the projected augmented plane-wave (PAW)[40] method as implemented in the Vienna ab initio simulation package (VASP).[41] Generalized gradient approximation (GGA) given by Perdew−Burke−Ernzerhof (PBE) was adopted for exchange−correlation functionals.[42] Considering the strongly correlated electrons in the partially filled d subshells, we use the GGA + U method introduced by Dudarev et al.[43] with U_{eff} = 4 eV for Ni d orbitals. The electronic wave functions are expanded using a plane-wave basis set with a cutoff energy of 500 eV. For 2D monolayer system, a vacuum space of 20 Å along the z direction is adopted to avoid interactions between two neighboring images. The Γ-centered Monkhorst−Pack[44−46] point scheme with 8 × 8 × 1 and 4 × 8 × 1 grid meshes is used to sample the reciprocal space of the primitive cell and the 2 × 1 super cell, respectively. For the bulk crystals, the DFT-D3 method by Grimme[47] is used to account for the weak vdW interactions between different layers. During the optimization, both the lattice constants and positions of all

DOI: 10.1021/acsomega.9b00056
ACS Omega 2019, 4, 5714−5721

atoms are relaxed without any symmetry restriction until the Hellmann−Feynman force on each atom is less than 0.01 eV $Å^{-1}$. The convergent criterion for the total energy is set as 1×10^{-5} eV.

AUTHOR INFORMATION

Corresponding Authors

*E-mail: dawnhcx@gmail.com (C.H.).
*E-mail: ekan@njust.edu.cn (E.K.).

ORCID

Chengxi Huang: 0000-0003-1491-3954
Erjun Kan: 0000-0003-0433-4190

Notes

The authors declare no competing financial interest.

ACKNOWLEDGMENTS

The work is supported by the NSFC (51522206, 11774173), the Fundamental Research Funds for the Central Universities (no. 30915011203). C.H. and E.K. acknowledge the support from the Tianjing Supercomputer Centre and Shanghai Supercomputer Center.

REFERENCES

(1) Novoselov, K. S.; Geim, A. K.; Morozov, S. V.; Jiang, D.; Zhang, Y.; Dubonos, S. V.; Grigorieva, I. V.; Firsov, A. A. Electric Field Effect in Atomically Thin Carbon Films. *Science* **2004**, *306*, 666−669.

(2) Han, W.-Q.; Wu, L.; Zhu, Y.; Watanabe, K.; Taniguchi, T. Structure of Chemically Derived Mono- and Few-Atomic-Layer Boron Nitride Sheets. *Appl. Phys. Lett.* **2008**, *93*, 223103−223105.

(3) Wang, Q. H.; Kalantar-Zadeh, K.; Kis, A.; Coleman, J. N.; Strano, M. S. Electronics and Optoelectronics of Two-Dimensional Transition Metal Dichalcogenides. *Nat. Nanotechnol.* **2012**, *7*, 699−712.

(4) Youngblood, N.; Chen, C.; Koester, S. J.; Li, M. Waveguide-Integrated Black Phosphorus Photodetector with High Responsivity and Low Dark Current. *Nat. Photonics* **2015**, *9*, 247−252.

(5) Fert, A. Nobel Lecture: Origin, Development, and Future of Spintronics. *Rev. Mod. Phys.* **2008**, *80*, 1517−1530.

(6) Mermin, N. D.; Wagner, H. Absence of Ferromagnetism or Antiferromagnetism in One- or Two-dimensional Isotropic Heisenberg Models. *Phys. Rev. Lett.* **1966**, *17*, 1133−1136.

(7) Gong, C.; Li, L.; Li, Z.; Ji, H.; Stern, A.; Xia, Y.; Cao, T.; et al. Discovery of Intrinsic Ferromagnetism in Two-Dimensional van der Waals Crystals. *Nature* **2017**, *546*, 265−269.

(8) Huang, B.; Clark, G.; Navarro-Moratalla, E.; Klein, D. R.; Cheng, R.; Seyler, K. L.; Zhong, D.; et al. Layer-Dependent Ferromagnetism in a van der Waals Crystal Down to The Monolayer Limit. *Nature* **2017**, *546*, 270−273.

(9) Krasheninnikov, A. V.; Lehtinen, P. O.; Foster, A. S.; Pyykkö, P.; Nieminen, R. M. Embedding Transition-Metal Atoms in Graphene: Structure, Bonding, and Magnetism. *Phys. Rev. Lett.* **2009**, *102*, 126807.

(10) Zhou, Y.; Su, Q.; Wang, Z.; Deng, H.; Zu, X. Controlling magnetism of MoS_2 Sheets by Embedding Transition-Metal Atoms and Applying Strain. *Phys. Chem. Chem. Phys.* **2013**, *15*, 18464−18470.

(11) Nair, R. R.; Sepioni, M.; Tsai, I.-L.; Lehtinen, O.; Keinonen, J.; Krasheninnikov, A. V.; Thomson, T.; Geim, A. K.; Grigorieva, I. V. Spin-Half Paramagnetism in Graphene Induced by Point Defects. *Nat. Phys.* **2012**, *8*, 199−202.

(12) Du, A.; Chen, Y.; Zhu, Z.; Amal, R.; Lu, G. Q.; Smith, S. C. Dots Versus Antidots: Computational Exploration of Structure,Magnetism, and Half-Metallicity in Boron-Nitride Nanostructures. *J. Am. Chem. Soc.* **2009**, *131*, 17354−17359.

(13) Wang, H.; Zhang, J.; Hang, X.; Zhang, X.; Xie, J.; Pan, B.; Xie, Y. Half-Metallicity in Single-Layered Manganese Dioxide Nanosheets by Defect Engineering. *Angew. Chem., Int. Ed.* **2015**, *127*, 1211−1215.

(14) Bonilla, M.; Kolekar, S.; Ma, Y.; Diaz, H. C.; Kalappattil, V.; Das, R.; Eggers, T.; Gutierrez, H. R.; Phan, M.-H.; Batzill, M. Strong room-Temperature Ferromagnetism in VSe_2 Monolayers on van der Waals Substrates. *Nat. Nanotechnol.* **2018**, *13*, 289−293.

(15) O'Hara, D. J.; Zhu, T.; Trout, A. H.; Ahmed, A. S.; Luo, Y. K.; Lee, C. H.; et al. Room Temperature Intrinsic Ferromagnetism in Epitaxial Manganese Selenide Films in the Monolayer Limit. *Nano Lett.* **2018**, *18*, 3125−3131.

(16) Wang, X.; Du, K.; Liu, Y. Y. F.; Hu, P.; Zhang, J.; Zhang, Q.; et al. Raman Spectroscopy of Atomically Thin Two-Dimensional Magnetic Iron Phosphorus trisulfide ($FePS_3$) Crystals. *2D Mater.* **2016**, *3*, 031009.

(17) Kan, M.; Zhou, J.; Sun, Q.; Kawazoe, Y.; Jena, P. The Intrinsic Ferromagnetism in a MnO_2 Monolayer. *J. Phys. Chem. Lett.* **2013**, *4*, 3382−3386.

(18) Liu, H.; Neal, A. T.; Zhu, Z.; Luo, Z.; Xu, X.; Tománek, D.; Ye, P. D. Phosphorene: An Unexplored 2D Semiconductor with a High Hole Mobility. *ACS Nano* **2014**, *8*, 4033−4041.

(19) Nicolosi, V.; Chhowalla, M.; Kanatzidis, M. G.; Strano, M. S.; Coleman, J. N. Liquid Exfoliation of Layered Materials. *Science* **2013**, *340*, 1226419.

(20) Sachs, B.; Wehling, T. O.; Novoselov, K. S.; Lichtenstein, A. I.; Katsnelson, M. I. Ferromagnetic Two-Dimensional Crystals: Single Layers of K_2CuF_4. *Phys. Rev. B* **2013**, *88*, 201402.

(21) Zacharia, R.; Ulbricht, H.; Hertel, T. Interlayer Cohesive Energy of Graphite from Thermal Desorption of Polyaromatic Hydrocarbons. *Phys. Rev. B* **2004**, *69*, 155406.

(22) Ziambaras, E.; Kleis, J.; Schröder, E.; Hyldgaard, P. Potassium Intercalation in Graphite: A Van der Waals Density-Functional Study. *Phys. Rev. B* **2007**, *76*, 155425.

(23) Li, X.; Wu, X.; Yang, J. Half-Metallicity in $MnPSe_3$ Exfoliated Nanosheet with Carrier Doping. *J. Am. Chem. Soc.* **2014**, *136*, 11065−11069.

(24) Lee, C.; Wei, X.; Kysar, J. W.; Hone, J. Measurement of the Elastic Properties and Intrinsic Strength of Monolayer Graphene. *Science* **2008**, *321*, 385−388.

(25) Booth, T. J.; Blake, P.; Nair, R. R.; Jiang, D.; Hill, E. W.; Bangert, U.; et al. Macroscopic Graphene Membranes and their Extraordinary Stiffness. *Nano Lett.* **2008**, *8*, 2442−2446.

(26) (a) Mounet, N.; Gibertini, M.; Schwaller, P.; Campi, D.; Merkys, A.; Marrazzo, A.; et al. Two-dimensional Materials from High-Throughput Computational Exfoliation of Experimentally Known Compounds. *Nat. Nanotechnol.* **2018**, *13*, 246−252. (b) Kulish, V. V.; Huang, W. Single-layer metal halides MX_2 (X= Cl, Br, I): Stability and tunable magnetism from first principles and Monte Carlo simulations. *J. Mater. Chem. C* **2017**, *5*, 8734−8741.

(27) Huang, C.; Feng, J.; Wu, F.; Ahmed, D.; Huang, B.; Xiang, H.; Deng, K.; Kan, E. Toward Intrinsic Room-Temperature Ferromagnetism in Two-Dimensional Semiconductors. *J. Am. Chem. Soc.* **2018**, *140*, 11519−11525.

(28) Liu, J.; Sun, Q.; Kawazoe, Y.; Jena, P. Exfoliating Biocompatible Ferromagnetic Cr-trihalide Monolayers. *Phys. Chem. Chem. Phys.* **2016**, *18*, 8777−8784.

(29) Zhou, Y.; Lu, H.; Zu, X.; Gao, F. Evidencing The Existence of Exciting Half-Metallicity in Two-Dimensional $TiCl_3$ and VCl_3 Sheets. *Sci. Rep.* **2016**, *6*, 19407.

(30) Ising, E. Beitrag zur Theorie des Ferromagnetismus. *Z. Phys.* **1925**, *31*, 253−258.

(31) Aguilera-Granja, F.; Morán-López, J. L. Ising Model of Phase Transitions in Ultrathin Films. *Solid State Commun.* **1990**, *74*, 155−158.

(32) Miao, N.; Xu, B.; Zhu, L.; Zhou, J.; Sun, Z. 2D Intrinsic Ferromagnets from van der Waals Antiferromagnets. *J. Am. Chem. Soc.* **2018**, *140*, 2417−2420.

(33) Liu, J.; Sun, Q. Enhanced Ferromagnetism in a $Mn_3C_{12}N_{12}H_{12}$ Sheet. *Chem. Phys. Chem.* **2015**, *16*, 614−620.

DOI: 10.1021/acsomega.9b00056
ACS Omega 2019, 4, 5714−5721

(34) Zhou, J.; Sun, Q. Magnetism of Phthalocyanine-Based Organometallic Single Porous Sheet. *J. Am. Chem. Soc.* **2011**, *133*, 15113−15119.
(35) Sato, K.; Bergqvist, L.; Kudrnovský, J.; Dederichs, P. H.; Eriksson, O.; Turek, I.; Sanyal, B.; Bouzerar, G.; Katayama-Yoshida, H.; Dinh, V. A.; et al. First-Principles Theory of Dilute Magnetic Semiconductors. *Rev. Mod. Phys.* **2010**, *82*, 1633−1690.
(36) Li, X.; Yang, J. $CrXTe_3$ (X = Si, Ge) Nanosheets: Two Dimensional Intrinsic Ferromagnetic Semiconductors. *J. Mater. Chem. C* **2014**, *2*, 7071−7076.
(37) Zhang, J.; Jia, S.; Kholmanov, I.; Dong, L.; Er, D.; Chen, W.; et al. Janus Monolayer Transition-Metal Dichalcogenides. *ACS Nano* **2017**, *11*, 8192−8198.
(38) Li, R.; Cheng, Y.; Huang, W. Recent Progress of Janus 2D Transition Metal Chalcogenides: From Theory to Experiments. *Small* **2018**, *14*, 1802091.
(39) Zhang, C.; Nie, Y.; Sanvito, S.; Du, A. First-Principles Prediction of a Room-Temperature Ferromagnetic Janus VSSe Monolayer with Piezoelectricity, Ferroelasticity, and Large Valley Polarization. *Nano Lett.* **2019**, *19*, 1366−1370.
(40) Kresse, G.; Joubert, D. From Ultrasoft Pseudopotentials to the Projector Augmented-Wave Method. *Phys. Rev. B* **1999**, *59*, 1758−1775.
(41) Kresse, G.; Furthmüller, J. Efficient Iterative Schemes for ab initio Total-Energy Calculations Using a Plane-Wave Basis Set. *Phys. Rev. B* **1996**, *54*, 11169−11186.
(42) Perdew, J. P.; Burke, K.; Ernzerhof, M. Generalized Gradient Approximation Made Simple. *Phys. Rev. Lett.* **1996**, *77*, 3865−3868.
(43) Dudarev, S. L.; Botton, G. A.; Savrasov, S. Y.; Humphreys, C. J.; Sutton, A. P. Electron-Energy-Loss Spectra and the Structural Stability of Nickel Oxide: An LSDA+U Study. *Phys. Rev. B* **1998**, *57*, 1505−1509.
(44) Monkhorst, H. J.; Pack, J. D. Special Points for Brillouin-Zone Integrations. *Phys. Rev. B* **1976**, *13*, 5188−5192.
(45) Chadi, D. J.; Cohen, M. L. Special Points in the Brillouin Zone. *Phys. Rev. B* **1973**, *8*, 5747−5753.
(46) Baldereschi, A.; Tosatti, E. Mean-Value Point and Dielectric Properties of Semiconductors and Insulators. *Phys. Rev. B* **1978**, *17*, 4710−4717.
(47) Grimme, S. Semiempirical GGA-type Density Functional Constructed with a Long-Range Dispersion Correction. *J. Comput. Chem.* **2006**, *27*, 1787−1799.

DOI: 10.1021/acsomega.9b00056
ACS Omega 2019, 4, 5714−5721